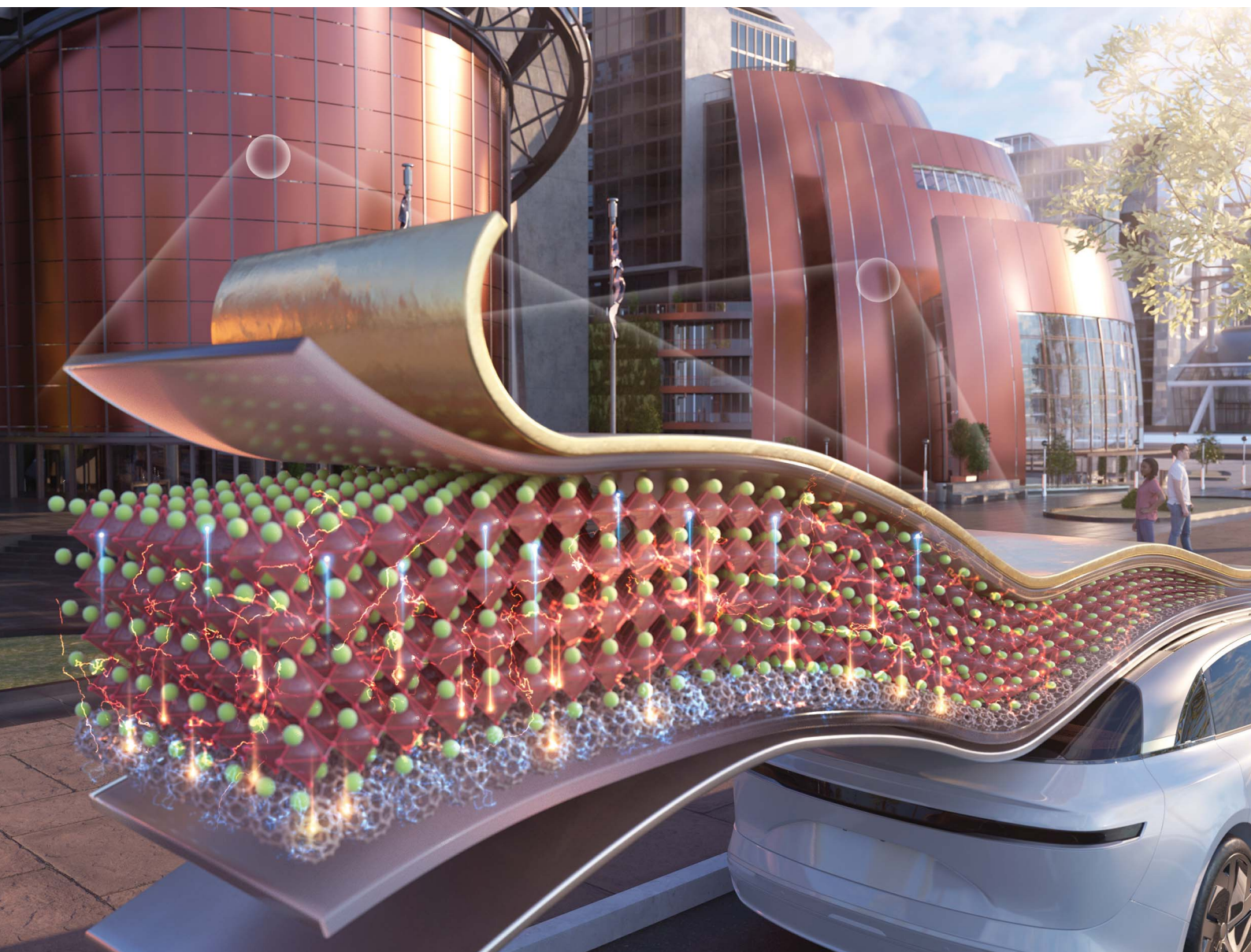


# EES Solar

rsc.li/EESSolar








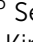


ISSN 3033-4063

## PAPER

Dong Ha Kim, Hae-Seok Lee *et al.*  
Enhanced bending stability of flexible perovskite solar cells  
on stainless steel substrates *via* C<sub>60</sub> buffer layer integration


Cite this: *EES Sol.*, 2025, 1, 736

# Enhanced bending stability of flexible perovskite solar cells on stainless steel substrates via C<sub>60</sub> buffer layer integration†

Hyun Jeong Lee, <sup>‡a</sup> Kyunghwan Kim, <sup>‡b</sup> Solhee Lee, <sup>b</sup> Dowon Pyun, <sup>b</sup> Ji-Seong Hwang, <sup>b</sup> Jiyeon Nam, <sup>b</sup> Sujin Cho, <sup>b</sup> Seok-Hyun Jeong, <sup>b</sup> Donghwan Kim, <sup>b</sup> Yoonmook Kang, <sup>cd</sup> Dong Ha Kim <sup>\*aefgh</sup> and Hae-Seok Lee <sup>\*cd</sup>

Flexible perovskite solar cells (PSCs) based on stainless steel (SS) substrates offer a highly promising platform for next-generation Building-Integrated Photovoltaics (BIPV) and Vehicle-Integrated Photovoltaics (VIPV), owing to their superior durability, mechanical strength, and thermal resilience. However, achieving long-term operational stability under bending stress remains a significant hurdle. In this work, we identify fractures in the TiO<sub>2</sub> electron transport layer as the dominant source of performance degradation under mechanical deformation. To address this issue, we introduce a C<sub>60</sub> buffer layer atop the TiO<sub>2</sub>, which serves dual functions: mechanical protection and enhanced interfacial charge extraction. The C<sub>60</sub> layer functions by redistributing strain through a shift of the neutral axis closer to the TiO<sub>2</sub> layer and by passivating interfacial trap states, as confirmed by SEM, AFM, PL, TRPL, and EIS analyses. As a result, SS-based PSCs with an optimized 20 nm C<sub>60</sub> layer demonstrate a remarkable ~5% increase in PCE before bending and an ~92.84% improvement in PCE retention after bending, compared to control devices. Furthermore, devices maintained superior performance over 100 bending cycles and continuous bending for 100 hours. These findings establish the C<sub>60</sub> buffer layer as a powerful strategy for enabling flexible PSCs with both high efficiency and mechanical reliability, accelerating their practical deployment in BIPV and VIPV systems where mechanical stress is unavoidable.

Received 21st March 2025

Accepted 7th July 2025

DOI: 10.1039/d5el00037h

rsc.li/EESolar

## Broader context

Flexible and durable perovskite solar cells (PSCs) are essential for emerging applications in building-integrated photovoltaics (BIPV) and vehicle-integrated photovoltaics (VIPV). This study addresses the mechanical and electrical challenges faced by stainless steel (SS)-based PSCs under bending conditions and proposes a strategy to enhance their stability and efficiency. By incorporating a 20 nm thick C<sub>60</sub> buffer layer, we significantly improved bending durability and charge extraction efficiency, mitigating damage to the TiO<sub>2</sub> layer. The optimized SS-based PSCs achieved a 92.84% improvement in PCE retention after bending, demonstrating the potential of C<sub>60</sub> integration as a viable approach for robust and flexible PSCs. These findings contribute to the advancement of high-performance, flexible photovoltaics for next-generation energy applications.

<sup>a</sup>Department of Chemistry and Nanoscience, Ewha Womans University, 52, Ewhayeodae-gil, Seodaemun-gu, Seoul 03760, Republic of Korea. E-mail: dhkim@ewha.ac.kr

<sup>b</sup>Department of Materials and Engineering, Korea University, Seoul 02841, Republic of Korea

<sup>c</sup>Graduate School of Energy and Environment (KU-KIST Green School), Korea University, Seoul 02841, Republic of Korea. E-mail: lhseok@korea.ac.kr

<sup>d</sup>Department of Integrative Energy Engineering, Korea University, Seoul 02841, Republic of Korea

<sup>e</sup>College of Medicine, Ewha Womans University, 25, Magokdong-ro 2-gil, Gangseo-gu, Seoul 07804, Republic of Korea

<sup>f</sup>Graduate Program in Innovative Biomaterials Convergence, Ewha Womans University, 52 Ewhayeodae-gil, Seodaemun-gu, Seoul 03760, Republic of Korea

<sup>g</sup>Basic Sciences Research Institute (Priority Research Institute), Ewha Womans University, 52, Ewhayeodae-gil, Seodaemun-gu, Seoul 03760, Republic of Korea

<sup>h</sup>Nanobio Energy Materials Center (National Research Facilities and Equipment Center), Ewha Womans University, 52, Ewhayeodae-gil, Seodaemun-gu, Seoul 03760, Republic of Korea

† Electronic supplementary information (ESI) available. See DOI: <https://doi.org/10.1039/d5el00037h>

‡ These authors contributed equally to the work.





## Introduction

Recent years have witnessed substantial progress in the development of flexible solar cells tailored for Building-Integrated Photovoltaics (BIPV) and Vehicle-Integrated Photovoltaics (VIPV).<sup>1–4</sup> Among these advancements, stainless steel (SS)-based perovskite solar cells (PSCs) have garnered significant attention due to their remarkable durability, superior mechanical strength, and flexibility, which surpass those of conventional flexible substrates.<sup>5–8</sup> These attributes render SS-based PSCs highly suitable for demanding applications in BIPV and VIPV, where structural stability under mechanical stress is essential.<sup>9–12</sup> Despite these advantages, SS-based PSCs continue to face critical challenges, particularly efficiency degradation when subjected to bending and mechanical stress. While SS-based PSCs have emerged as a promising alternative to overcome these limitations, the majority of research to date has remained focused on polymer-based substrates, such as polyethylene terephthalate (PET) and polyethylene naphthalate (PEN).<sup>13–16</sup> Li *et al.* reported a flexible PSCs incorporating a bio-inspired multisite polymer, which achieved a power conversion efficiency (PCE) of 24.43% and retained 94.1% of its initial performance after 10 000 bending cycles under high humidity conditions.<sup>17</sup> Similarly, Chalkias *et al.* demonstrated a carbon-based flexible PSCs fabricated under ambient air, achieving a PCE of 20.09% and maintaining mechanical stability over 5000 bending cycles.<sup>18</sup> Furthermore, Dong *et al.* developed a fully printed flexible PSCs module that preserved 95% of its original efficiency after 3000 cycles of mechanical deformation.<sup>19</sup> These studies collectively highlight key strategies to simultaneously enhance efficiency and mechanical robustness, including the introduction of elastic or ductile interlayers, surface modifications to improve interfacial adhesion and stress distribution, and structural designs that position functional layers near the neutral mechanical plane.

In environments such as construction and automotive applications, solar cells are frequently exposed to a range of stressors, including temperature fluctuations, physical impacts, prolonged moisture, and ultraviolet (UV) radiation.<sup>20</sup> The inherent mechanical strength of stainless steel offers a robust foundation capable of withstanding bending and deformation, ensuring the structural and functional stability of PSCs under such adverse conditions. Research into SS-based PSCs has shown considerable progress in recent years. For instance, in 2022, Feleki *et al.* achieved a PCE of 16.5% in p–i–n structured SS-based PSCs fabricated on polymer-coated SS substrates.<sup>5</sup> Zheng *et al.* improved the PCE to 17.1% in 2023 by introducing an 80 nm indium tin oxide (ITO) interlayer and applying surface passivation techniques.<sup>7</sup> In 2024, Zhou *et al.* further enhanced SS-based PSC performance, achieving a PCE of 20.2% by incorporating single crystals into the precursor solution to reduce perovskite defects and passivating the surface of the perovskite film.<sup>8</sup>

Despite these advancements, efficiency degradation under mechanical stress remains a persistent challenge for SS-based PSCs. Bending and deformation can lead to micro-crack

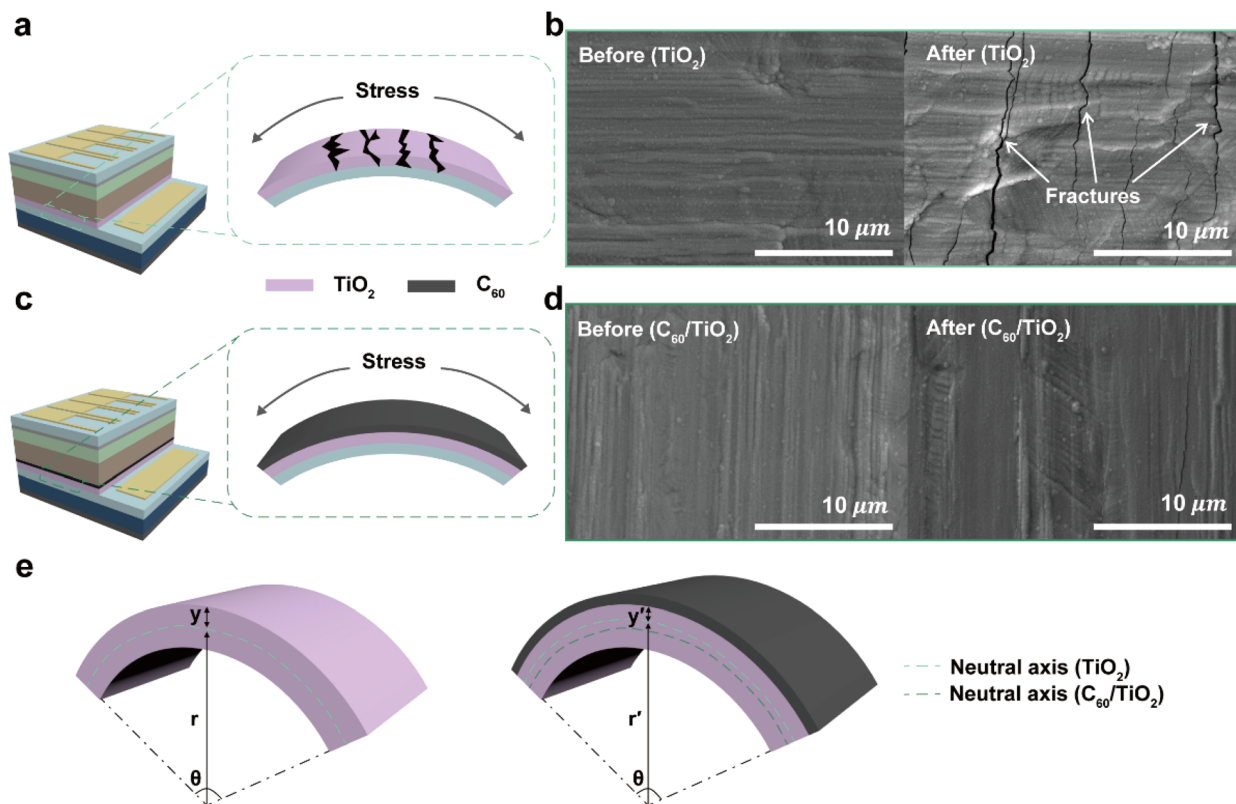
formation, delamination within the functional layers, and hindered charge transport, ultimately resulting in power loss.<sup>21,22</sup> Moreover, mechanical stress exacerbates ion migration and layer instability within the perovskite material, further reducing operational efficiency. Therefore, improving the mechanical and operational stability of SS-based PSCs under bending conditions remains a pivotal research focus. While significant progress has been made in advancing SS-based PSCs, there is a notable gap in understanding the specific causes of efficiency degradation under bending conditions. Investigating these mechanisms is essential for enabling the practical application of SS-based PSCs in BIPV and VIPV, where mechanical robustness and long-term performance are critical.

In this work, we address the key mechanical limitations of SS-based PSCs, which are highly promising for real-world flexible photovoltaic applications. We identify the fracture of the TiO<sub>2</sub> electron transport layer as a critical factor contributing to performance degradation under bending conditions and propose the integration of a C<sub>60</sub> buffer layer as a dual-function solution that provides both mechanical stress relief and enhanced interfacial charge extraction. Unlike conventional approaches that focus solely on either flexibility or efficiency, our strategy simultaneously enhances both mechanical robustness and electronic performance. This study presents a novel design principle for realizing high-efficiency, mechanically stable SS-based PSCs, paving the way for their practical implementation in BIPV and VIPV. Notably, the optimized device incorporating a 20 nm C<sub>60</sub> buffer layer exhibited a PCE of 17.51% before bending and retained approximately 92.84% of its initial performance after bending.

## Results and discussion

To explore the causes of efficiency degradation in SS-based PSCs, scanning electron microscopy (SEM) measurements were performed to observe structural changes induced by bending. The samples were subjected to a bending diameter of 10 mm for 1 hour prior to analysis. Fig. 1a and c present schematic representations of surface damage phenomena observed without and with the incorporation of a C<sub>60</sub> buffer layer, respectively. As depicted in Fig. 1b, the TiO<sub>2</sub> layer exhibits a smooth surface prior to bending, while clear fractures appear after bending. Conversely, when a C<sub>60</sub> buffer layer is incorporated, as shown in Fig. 1d, the TiO<sub>2</sub> layer remains intact, exhibiting no fractures even after bending. In addition, atomic force microscopy (AFM) measurements were conducted to evaluate surface roughness. The TiO<sub>2</sub> film displayed roughness values of 49 nm before bending and 144 nm after bending, indicating significant surface damage due to bending (Fig. S1a and S1c, ESI†). In contrast, the C<sub>60</sub>/TiO<sub>2</sub> hybrid film showed roughness values of 15 nm before bending and 44 nm after bending, maintaining a significantly smoother surface compared to the single TiO<sub>2</sub> film (Fig. S1b and S1d, ESI†). Although both films displayed a similar relative increase in roughness, the absolute roughness of the C<sub>60</sub>/TiO<sub>2</sub> film remained significantly lower. It should be noted, however, that the AFM measurements represent localized surface





**Fig. 1** Surface damage assessment of  $\text{TiO}_2$  due to bending: (a) schematic illustration showing the surface damage of  $\text{TiO}_2$  after bending. (c) Schematic illustration of  $\text{C}_{60}/\text{TiO}_2$  deposited on SS-based PSCs after bending. (b) SEM images of  $\text{TiO}_2$  before and after bending. (d) SEM images of  $\text{C}_{60}/\text{TiO}_2$  deposited on SS-based PSCs before and after bending. (e) Schematic illustration of the neutral axis shifts in SS-based PSCs without and with the  $\text{C}_{60}$  buffer layer.

characteristics and may not comprehensively reflect the overall stress distribution within the complete multilayered device under bending conditions. Therefore, the roughness data are used here as supportive indicators of morphological trends rather than as definitive predictors of mechanical failure. Further analysis of the indium tin oxide thin film using the same methodology revealed no fractures in the ITO layer after bending (Fig. S2, ESI†). These results indicate that preventing fractures in the  $\text{TiO}_2$  layer is crucial for enhancing the efficiency and mechanical stability of SS-based PSCs.

The changes experienced by each layer in multilayered structures before and after bending are illustrated in Fig. S3, ESI†. In this analysis,  $y$  represents the distance from the neutral axis,  $R$  denotes the radius relative to the neutral axis, and  $\theta$  indicates the central angle with respect to the neutral axis. When bending is applied, each layer undergoes stress ( $\sigma$ )—the force exerted to maintain its shape against external forces—and strain ( $\varepsilon$ ), the deformation resulting from these forces.<sup>23–27</sup> Specifically, layers above the neutral axis experience tensile forces, while layers below it are subjected to compressive forces. According to the stress–strain behaviour of ceramic materials, exceeding a certain stress threshold causes the material to lose its ability to return to its original state, ultimately leading to failure.<sup>28</sup> The relationships between  $\varepsilon$  and  $\sigma$  in the layers during bending are described by the equations shown in Fig. 1e.<sup>21,29,30</sup>

$$\varepsilon = \frac{(r + y)\theta - r\theta}{r\theta} = -\frac{y}{r} \quad (1)$$

$$\sigma = E \times \varepsilon = -E \times \frac{y}{r} \quad (2)$$

While eqn (1) and (2) provide a fundamental analytical framework for evaluating strain and stress distributions in multilayer structures, they are based on idealized assumptions, including uniform Young's modulus and linear elastic behavior. Notably, the Young's modulus values used in the analysis are derived from bulk materials reported in the literature and may not accurately reflect the mechanical response of nanostructured thin films under bending deformation. As such, the results should be interpreted qualitatively, emphasizing relative trends rather than absolute values.

When a  $\text{C}_{60}$  layer is introduced on top of the  $\text{TiO}_2$  layer, the neutral axis ( $N$ ) of the layered structure is theoretically expected to shift slightly. The position of the neutral axis can be estimated using eqn (3), assuming ideal layer homogeneity and isotropy:<sup>21,31</sup>



$$N = \frac{\sum_{i=1}^n E_i t_i \left[ \left( \sum_{j=1}^i t_j \right) - \frac{t_i}{2} \right]}{\sum_{i=1}^n E_i t_i} \quad (3)$$

where  $E$  is Young's modulus,  $n$  is number of layer, and  $t$  is thickness of layer. During bending, layers above the neutral axis experience tensile forces, increasing surface stress. Consequently, layers with a higher Young's modulus are more susceptible to damage, as Young's modulus quantifies the material's elastic deformation under applied stress ( $\sigma$ ). Materials with higher Young's modulus values are more prone to failure than those with lower values. Among the components of SS-based PSCs,  $\text{TiO}_2$  has the highest Young's modulus of 151 GPa (Table S1, ESI†). For the  $\text{TiO}_2$  and  $\text{C}_{60}/\text{TiO}_2$  composite structures, the neutral axis values are 25.00 nm and 29.94 nm, respectively, indicating that the  $\text{C}_{60}$  buffer layer slightly shifts the N. The  $\varepsilon$  and  $\sigma$  values for the  $\text{TiO}_2$  layer are  $5.00 \times 10^{-6}$  and  $7.55 \times 10^{-4}$  GPa, respectively. However, in the  $\text{C}_{60}/\text{TiO}_2$  composite structure, the  $\varepsilon$  and  $\sigma$  on the  $\text{C}_{60}$  layer are  $8.01 \times 10^{-6}$  and  $4.96 \times 10^{-4}$  GPa, respectively, while the values for the  $\text{TiO}_2$  layer decrease to  $4.01 \times 10^{-6}$  and  $6.05 \times 10^{-4}$  GPa, respectively. These reductions in  $\varepsilon$  and  $\sigma$  for the  $\text{TiO}_2$  layer—approximately 19.80% and 19.87%, respectively—significantly mitigate the risk of damage to the  $\text{TiO}_2$  thin film. This shift—together with

the relatively compliant nature of the  $\text{C}_{60}$  interface—may help reduce stress and strain within the brittle  $\text{TiO}_2$  layer during bending. This reduction is attributed to the shift in the neutral axis, which brings the  $\text{TiO}_2$  layer closer to the neutral plane, reducing  $\varepsilon$ , and to the ability of the  $\text{C}_{60}$  layer to absorb strain energy. Additionally, the low Young's modulus of the  $\text{C}_{60}$  layer enables it to effectively redistribute  $\sigma$ , providing enhanced protection for the  $\text{TiO}_2$  layer. The calculated values align closely with experimental results, underscoring the importance of introducing a buffer layer to improve the bending stability of SS-based PSCs.

To fabricate SS-based PSCs with a  $\text{C}_{60}$  buffer layer, the effects of  $\text{C}_{60}$  on the perovskite crystal structure were investigated. Fig. 2a shows the SS304 substrate and the chemical structure of  $\text{C}_{60}$  used as the buffer layer in this study. To investigate molecular interactions between perovskite and  $\text{C}_{60}$ , X-ray photoelectron spectroscopy (XPS) was conducted. In Fig. 2b, the binding energy peaks of  $\text{I } 3d_{5/2}$  and  $\text{I } 3d_{3/2}$  in the  $\text{MAPbI}_3$  film appear at 618.68 eV and 630.18 eV, respectively. For the  $\text{MAPbI}_3/\text{C}_{60}$  composite layer, these peaks shift to lower values by 0.4 eV and 0.2 eV, respectively, indicating strong electronic interactions between  $\text{C}_{60}$  and  $\text{I}^-$  ions due to charge transfer.<sup>32,33</sup> Similarly, Fig. 2c shows that the binding energy peaks of  $\text{Pb } 4f_{7/2}$  and  $\text{Pb } 4f_{5/2}$  in the  $\text{MAPbI}_3$  film, originally at 136.98 eV and 141.88 eV, shift to lower values by 0.3 eV and 0.4 eV, respectively, in the  $\text{MAPbI}_3/$

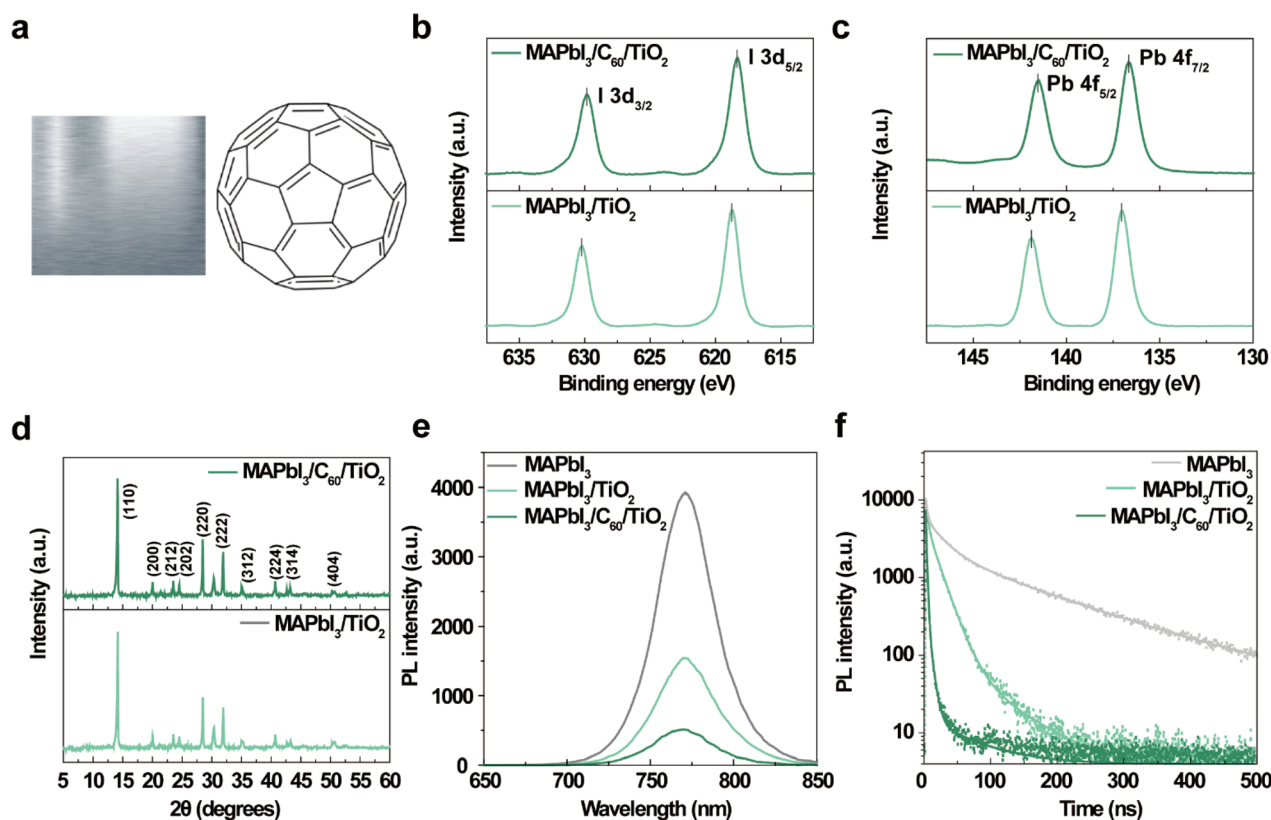


Fig. 2 Assessment of  $\text{C}_{60}$  characteristics and suitability as an interlayer: (a) image of SS substrate (left) and chemical structure of the  $\text{C}_{60}$  (right). (b) XPS spectra showing the I 3d peaks for  $\text{MAPbI}_3/\text{TiO}_2$  and  $\text{MAPbI}_3/\text{C}_{60}/\text{TiO}_2$  hybrid films. (c) XPS spectra showing the Pb 4f peaks for perovskite/ $\text{TiO}_2$  and  $\text{MAPbI}_3/\text{C}_{60}/\text{TiO}_2$  hybrid films. (d) XRD patterns of the  $\text{MAPbI}_3/\text{TiO}_2$  and  $\text{MAPbI}_3/\text{C}_{60}/\text{TiO}_2$  hybrid films. (e) Steady-state PL spectra and (f) time-resolved PL decay spectra of  $\text{MAPbI}_3/\text{TiO}_2$  and  $\text{MAPbI}_3/\text{C}_{60}/\text{TiO}_2$  hybrid films.



C<sub>60</sub> composite structure. This negative shift indicates strong interactions between C<sub>60</sub> and Pb<sup>2+</sup> ions, which contribute to defect passivation and enhanced interfacial charge transfer.<sup>32</sup> The crystallization of perovskite on the SS substrate was analyzed using X-ray diffraction (XRD), as shown in Fig. 2d. MAPbI<sub>3</sub>/C<sub>60</sub>/TiO<sub>2</sub> films and MAPbI<sub>3</sub>/TiO<sub>2</sub> films were prepared on SS substrates *via* the same deposition process. Both samples exhibit distinct diffraction peaks at 14.11° and 28.45°, corresponding to the (110) and (220) planes of MAPbI<sub>3</sub>, respectively.<sup>34,35</sup> The similarity in diffraction intensity between MAPbI<sub>3</sub>/C<sub>60</sub>/TiO<sub>2</sub> and MAPbI<sub>3</sub>/TiO<sub>2</sub> indicates that the incorporation of C<sub>60</sub> does not alter the crystallinity of the perovskite, confirming that a highly crystalline MAPbI<sub>3</sub> thin film can be formed on the SS substrate even in the presence of C<sub>60</sub>. Charge extraction properties were

further analyzed using steady-state photoluminescence (PL) and time-resolved photoluminescence (TRPL) measurements. Fig. 2e shows that all samples exhibit a PL peak at 770 nm, originating from MAPbI<sub>3</sub>. The PL quantum yield significantly decreases with the incorporation of TiO<sub>2</sub> and C<sub>60</sub>, demonstrating efficient charge carrier extraction from MAPbI<sub>3</sub> to C<sub>60</sub>.<sup>36,37</sup> The most pronounced PL quenching observed in the MAPbI<sub>3</sub>/C<sub>60</sub>/TiO<sub>2</sub> structure indicates superior carrier extraction facilitated by C<sub>60</sub>.<sup>38</sup> TRPL decay curves for MAPbI<sub>3</sub>, MAPbI<sub>3</sub>/TiO<sub>2</sub>, and MAPbI<sub>3</sub>/C<sub>60</sub>/TiO<sub>2</sub> samples are shown in Fig. 2f, with detailed lifetime values provided in Table S2.† For the MAPbI<sub>3</sub> sample, the fast lifetime ( $\tau_1$ ) and average lifetime ( $\tau_{ave}$ ) were calculated as 14.09 ns and 66.30 ns, respectively. With the introduction of the C<sub>60</sub> buffer layer, these values decreased to 8.24 ns and 52.34 ns, respectively,

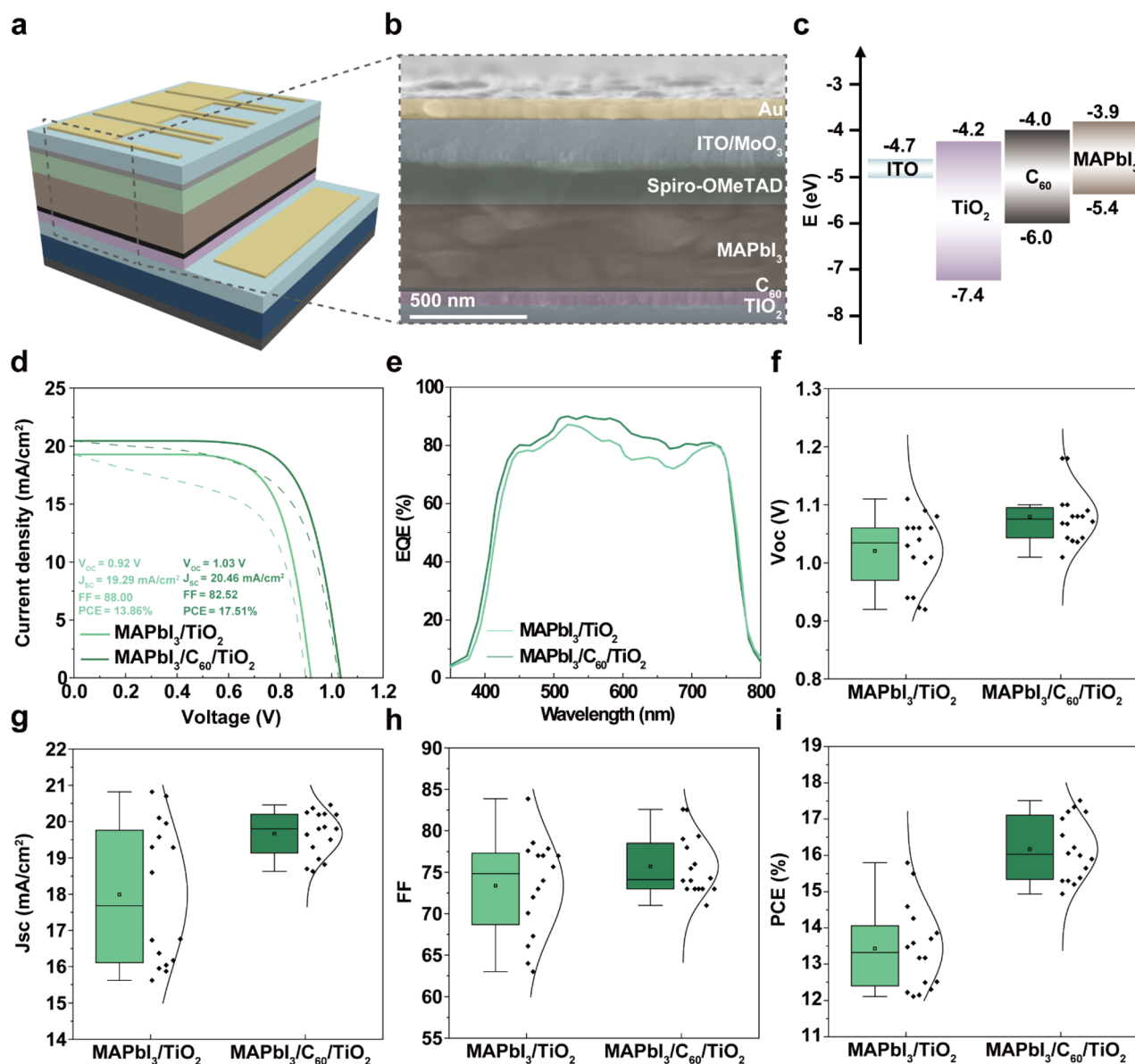


Fig. 3 Characterization and performance of SS-based PSCs: (a) schematic illustration of SS-based PSCs. (b) Cross-sectional SEM image of SS-based PSCs. (c) Energy level diagram of SS-based PSCs. (d) *J*–*V* characteristics of the most efficient devices with and without the C<sub>60</sub> layer (solid: reverse, dash: forward). (e) EQE plots of devices with and without the C<sub>60</sub> layer. (f–i) Statistical deviation of the photovoltaic parameters of the SS-based PSCs with and without the C<sub>60</sub> layer in the reverse scanning direction. (The error bar represents standard deviation from 16 devices).





indicating faster PL quenching and higher electron injection efficiency, ultimately enhancing photovoltaic performance.<sup>39</sup>

Fig. 3a shows the schematic of the fabricated SS-substrate-based PSC. The corresponding SEM cross-sectional image of the device is shown in Fig. 3b. The fabrication process of the device is illustrated in Fig. S4, ESI†. Due to the opaque nature of the SS substrate, light illumination was applied from the top side of the device. To enable this, a transparent ITO electrode was deposited on the top surface, followed by patterned Au deposition that served as the charge-collecting electrode while allowing light to pass through the ITO openings. This top-illumination configuration ensures accurate photovoltaic characterization of the SS-based PSCs (Fig. S5, ESI†). Fig. 3c shows the energy level diagram of the SS-based PSC, where the C<sub>60</sub> buffer layer efficiently extracts photogenerated electrons from the perovskite to the TiO<sub>2</sub> layer. This highlights the role of C<sub>60</sub> in facilitating charge separation and enhancing photovoltaic performance. To optimize C<sub>60</sub> thickness, devices with varying C<sub>60</sub> layers (5 nm, 10 nm, 20 nm, and 30 nm) were fabricated and measured under AM 1.5G illumination at 100 mW cm<sup>-2</sup> (1 sun). The perovskite crystal structure remained unaffected by C<sub>60</sub> variation (Fig. S6, ESI†). At 5 nm, the device achieved an open-circuit voltage (*V*<sub>oc</sub>) of 1.00 V, a short-circuit current density (*J*<sub>sc</sub>) of 21.48 mA cm<sup>-2</sup>, a fill factor (FF) of 68.90, and a power conversion efficiency of 14.83% (Fig. S7a, ESI†). At 10 nm, the device showed a slightly improved PCE of 16.07%, while *V*<sub>oc</sub>, *J*<sub>sc</sub>, and FF remained nearly unchanged (Fig. S7b, ESI†). The highest performance was achieved at 20 nm with a *V*<sub>oc</sub> of 1.03 V, a *J*<sub>sc</sub> of 20.46 mA cm<sup>-2</sup>, an FF of 82.52, and a peak PCE of 17.51% (Fig. 3d). At 30 nm, the PCE dropped to 14.75% due to a decrease in FF to 74.60 (Fig. S7c, ESI†). EQE spectra (Fig. S8, ESI†) confirmed that performance improved with increasing C<sub>60</sub> thickness up to 20 nm, but declined at 30 nm. Devices with thinner C<sub>60</sub> layers (5 nm and 10 nm) exhibited incomplete surface coverage on ITO, limiting performance. In contrast, the 20 nm C<sub>60</sub> layer achieved better surface coverage, improved charge extraction and overall efficiency. At 30 nm, the thicker C<sub>60</sub> layer partially absorbed sunlight, which reduced carrier generation and lowered performance.<sup>40</sup> These results indicate that 20 nm is optimal for C<sub>60</sub> thickness. Fig. 3d shows *J*-*V* curves comparing devices with and without 20 nm C<sub>60</sub>. The champion device achieved a high PCE of 17.51%, a *V*<sub>oc</sub> of 1.03 V, a *J*<sub>sc</sub> of 20.46 mA cm<sup>-2</sup>, and an FF of 82.52, significantly outperforming the device without the C<sub>60</sub> layer, which exhibited a PCE of 13.86%, a *V*<sub>oc</sub> of 0.92 V, a *J*<sub>sc</sub> of 19.29 mA cm<sup>-2</sup>, and an FF of 88.00. The 20 nm C<sub>60</sub> layer improved PCE by ~4%. To evaluate the hysteresis behavior of the devices, forward and reverse *J*-*V* scans were performed before bending. The device without the C<sub>60</sub> exhibited significant hysteresis, as evidenced by the large discrepancy between forward (dashed) and reverse (solid) scans. In contrast, the C<sub>60</sub>-buffered device showed a markedly reduced hysteresis, indicating improved interfacial charge extraction and suppressed ion migration at the TiO<sub>2</sub>/perovskite interface. Fig. 3e illustrates the EQE spectra in the wavelength range of 400–800 nm, showing higher EQE values for C<sub>60</sub>-incorporated devices. Box plots in Fig. 3f–i summarize performance data from 16 devices with and without C<sub>60</sub>. The 20 nm C<sub>60</sub> layer

slightly improved and stabilized *V*<sub>oc</sub> and *J*<sub>sc</sub>, due to reduced interfacial recombination and enhanced charge transport.<sup>41</sup> These trends align with PL spectra results (Fig. 2g). The most notable improvement was in PCE, mainly from stabilized FF along with slight *V*<sub>oc</sub> and *J*<sub>sc</sub> increases. These results confirm that C<sub>60</sub> improves both the interfacial quality and the overall photovoltaic performance.<sup>42</sup> To investigate the reasons behind the improved photovoltaic performance, SEM measurements were conducted (Fig. S9, ESI†). Perovskite grains grown on the C<sub>60</sub>/TiO<sub>2</sub> composite layer were significantly larger than those grown directly on the TiO<sub>2</sub> substrate. This is attributed to the C<sub>60</sub> buffer layer, which lowers interfacial energy between TiO<sub>2</sub> and the perovskite precursor solution. This reduction in interfacial energy improves wetting properties during the crystallization process, facilitating the formation of larger grains. Furthermore, the C<sub>60</sub> layer mitigates the surface roughness and defects of the TiO<sub>2</sub> substrate, providing a smoother surface that promotes unobstructed grain growth.<sup>43</sup> Additionally, the fullerene-based C<sub>60</sub> buffer layer serves as a passivation layer, effectively suppressing interfacial trap states<sup>44,45</sup> Besides electron transport, the C<sub>60</sub> layer passivated interfacial trap states and blocked I<sup>-</sup> ion migration, suppressing PbI<sub>2</sub> formation from reactions between I<sup>-</sup> and TiO<sub>2</sub> oxygen vacancies.<sup>46</sup>

To evaluate the potential application of C<sub>60</sub>-incorporated SS-based PSCs in BIPV and VIPV systems, the efficiency change under bending conditions was analyzed. Fig. 4a presents a schematic diagram of the fabricated SS-based PSCs, while Fig. 4b (left image) shows the fabricated SS-based PSCs and the right image illustrates the cell bent to a diameter of 10 mm. As shown in Fig. 4c, the SS-based PSC without C<sub>60</sub> incorporation, bent to a diameter of 10 mm, exhibited a *V*<sub>oc</sub> of 0.77 V, a *J*<sub>sc</sub> of 17.20 mA cm<sup>-2</sup>, a FF of 50.00, and a PCE of 6.70%. Compared to the unbent condition, the PCE decreased by approximately 7.16% after bending, indicating that the device is unsuitable for applications requiring various curved forms, such as those in BIPV and VIPV systems. In contrast, as shown in Fig. 4b, the C<sub>60</sub>-incorporated SS-based PSCs, bent to a diameter of 10 mm, achieved a *V*<sub>oc</sub> of 1.01 V, a *J*<sub>sc</sub> of 17.82 mA cm<sup>-2</sup>, a FF of 71.69, and a PCE of 12.92%. Compared to the unbent condition, the PCE exhibited a reduction of only 4.59%, which is significantly lower than the 7.16% reduction observed in devices without C<sub>60</sub> incorporation. Moreover, the PCE improved by 6.22% compared to devices prior to the introduction of C<sub>60</sub>. After bending, the difference in hysteresis became even more pronounced. As shown in Fig. 4c, the device without the C<sub>60</sub> buffer layer exhibited aggravated hysteresis behavior due to mechanical damage in the TiO<sub>2</sub> layer, whereas the device incorporating the C<sub>60</sub> buffer layer maintained superior mechanical and electrical stability. Fig. 4d illustrates the EQE values of cells with and without C<sub>60</sub> incorporation after bending to a diameter of 10 mm. It is evident that the EQE values of the cells without C<sub>60</sub> are significantly lower than those of the cells with C<sub>60</sub>. This finding suggests that C<sub>60</sub> not only enhances charge extraction through surface modification but also partially prevents degradation of the TiO<sub>2</sub> layer during bending. Fig. 4e–h show box plots comparing the *V*<sub>oc</sub>, *J*<sub>sc</sub>, FF, and PCE values of 16 SS-based PSCs with and without C<sub>60</sub> incorporation after bending to a diameter of 10 mm. When a 20 nm thick



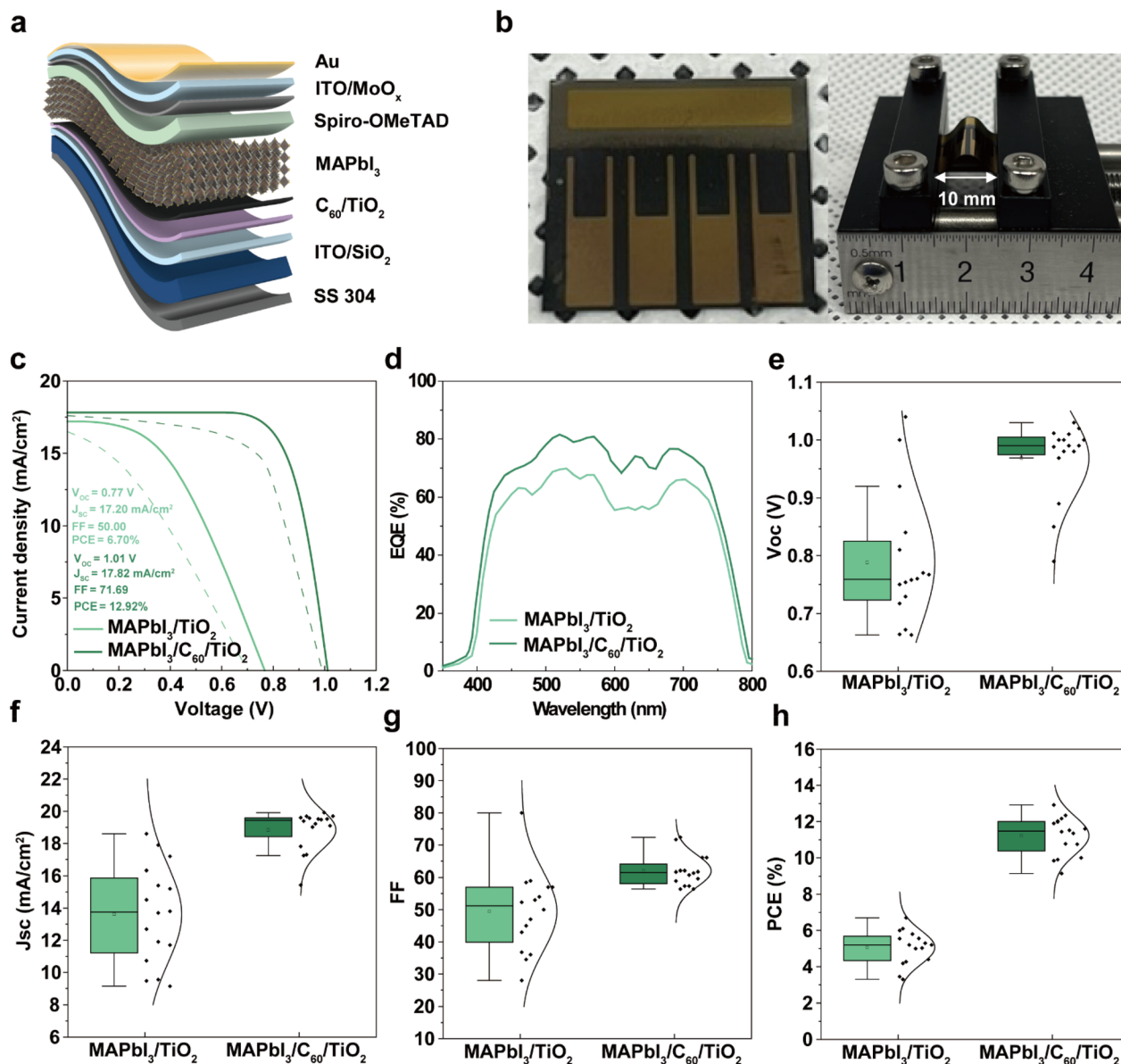


Fig. 4 Performance of SS-based flexible PSCs after bending: (a) schematic illustration of the SS-based flexible PSCs. (b) Images of SS-based flexible PSCs before and after bending. (c)  $J$ - $V$  characteristics of the most efficient devices after bending with and without the C<sub>60</sub> layer (solid: reverse, dash: forward). (d) EQE plots of devices after bending with and without the C<sub>60</sub> layer. (e–h) Statistical deviation of photovoltaic parameters of the SS-based PSCs after bending with and without the C<sub>60</sub> layer in the reverse scanning direction. (The error bar represents standard deviation from 16 devices).

C<sub>60</sub> layer was incorporated into SS-based PSCs, post-bending performance significantly improved compared to devices without the C<sub>60</sub> layer. While the FF showed a slight increase, noticeable enhancements were observed in the  $V_{oc}$ ,  $J_{sc}$ , and PCE. This improvement is attributed to the ability of C<sub>60</sub> to reduce defects at the TiO<sub>2</sub> interface, suppress interfacial recombination, and mitigate structural damage to the TiO<sub>2</sub> layer during bending. These properties allow the device to maintain high performance under mechanical stress. The incorporation of C<sub>60</sub> demonstrates significant potential for enabling the application of SS-based PSCs in BIPV and VIPV systems. The performance of previously reported SS-based PSCs has been summarized in Table S3, ESI.†

To understand why the incorporation of C<sub>60</sub> prevents performance degradation in SS-based PSCs after bending, the stress concentration factor ( $K$ ) was analyzed.<sup>47</sup>  $K$  quantifies the concentration of stress due to load transfer obstruction at specific points, such as notches and tips. The value of  $K$  is governed by the following equation:<sup>48,49</sup>

$$K = \frac{\sigma_{\max}}{\sigma_{\text{nom}}}, \quad K = 1 + \beta \cdot \left( \frac{R_p}{\lambda} \right) \quad (4)$$

$$\sigma_{\max} = \left( 1 + \beta \cdot \left( \frac{R_p}{\lambda} \right) \right) \cdot \sigma_{\text{nom}} \quad (5)$$





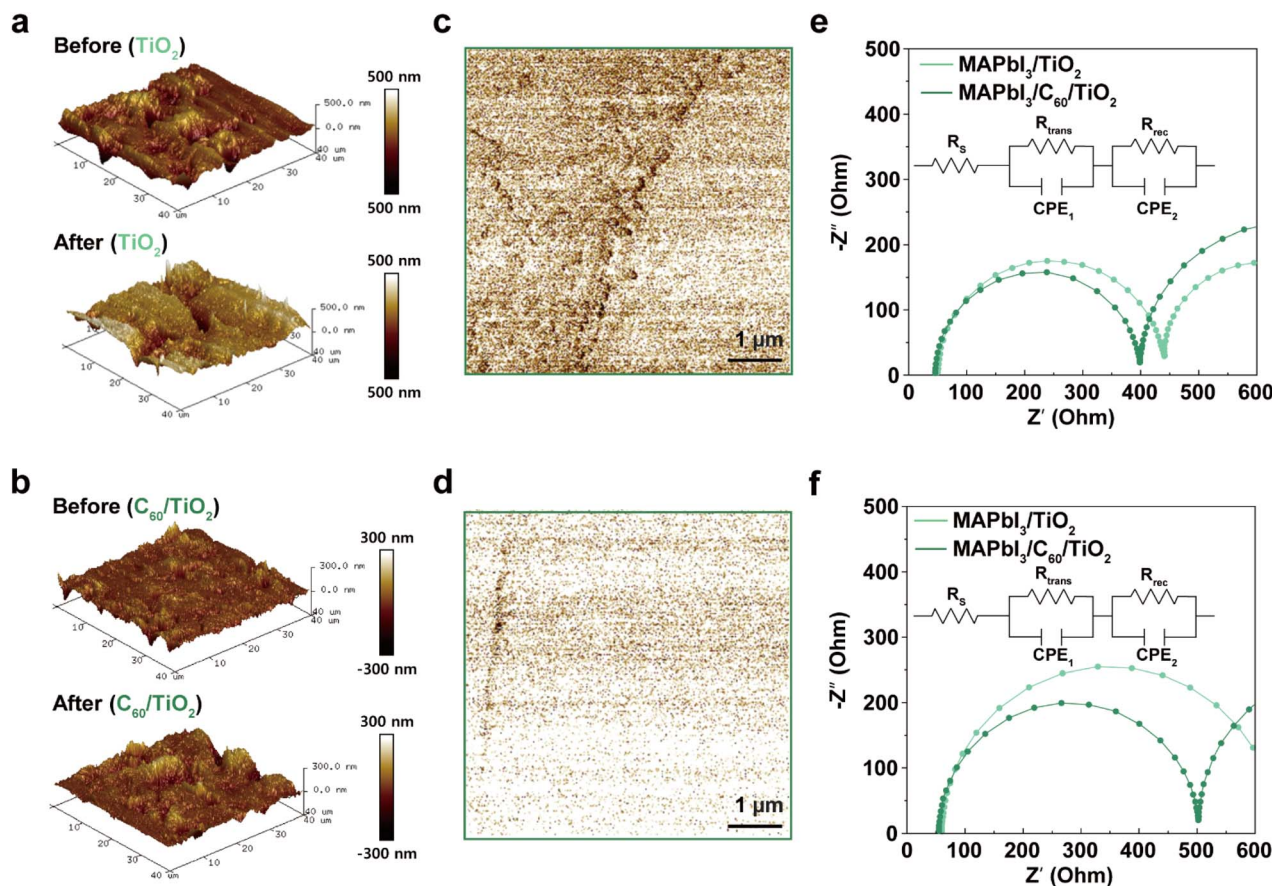


Fig. 5 Structural and electrical properties before and after bending: AFM 3D image of the device before and after bending (a) without (before RMS: 49.44 nm,  $R_a$ : 87.37 nm,  $R_p$ : 677.40 nm) (after RMS: 144.21 nm,  $R_a$ : 130.83 nm,  $R_p$ : 818.20 nm) (height range:  $-500$  to  $+500$  nm) and (b) with (before RMS: 15.92 nm,  $R_a$ : 10.71 nm,  $R_p$ : 293.00 nm) (after RMS: 44.23 nm,  $R_a$ : 30.02 nm,  $R_p$ : 386.90 nm) (height range:  $-300$  to  $+300$  nm)  $\text{C}_{60}$ . C-AFM image of the device after bending (c) without (min: 0.02 nA, max: 6.72 nA, mean: 2.38 nA) and (d) with (min: 0.19 nA, max: 10.43 nA, mean: 6.54 nA)  $\text{C}_{60}$ . Nyquist plot of SS-based PSCs without and with  $\text{C}_{60}$  (e) before and (f) after bending.

where  $R_p$  is the roughness peak-to-valley distance,  $\sigma_{\text{max}}$  is the maximum stress,  $\sigma_{\text{nom}}$  is nominal stress,  $\beta$  is the geometric influence coefficient and  $\lambda$  is a parameter related to surface characteristics. When  $R_p$  increases due to greater surface discontinuities or the formation of additional peaks and notches, the value of  $K$  also increases, as described by the equations. Therefore, reducing  $R_p$  is essential to minimize the stress applied to the  $\text{TiO}_2$  layers. Fig. 5a and b investigate the  $R_p$  values before and after bending, both with and without the incorporation of  $\text{C}_{60}$ . For devices without  $\text{C}_{60}$ , the  $R_p$  values were 677.40 nm and 818.20 nm before and after bending, respectively. However, with the introduction of  $\text{C}_{60}$ , the  $R_p$  values were significantly reduced to 293.00 nm before bending and 386.90 nm after bending, corresponding to reductions of 56.75% and 52.71%, respectively. This improvement in  $R_p$  effectively reduces the stress applied to the  $\text{TiO}_2$  layer, thereby preventing fractures during bending. These results underscore the critical role of  $\text{C}_{60}$  in enhancing the mechanical stability of SS-based PSCs under bending conditions. However, although these expressions provide a simplified estimation of local stress amplification due to surface features, they do not fully account for the complex interplay of interfacial adhesion, material

compliance, and multilayer coupling in the real device. The mechanical benefits of the  $\text{C}_{60}$  layer are not solely attributed to morphology smoothing. Rather, the  $\text{C}_{60}$  buffer is believed to act as a compliant interfacial layer that enhances mechanical coupling and accommodates local strain, while also passivating surface defects that may act as crack initiation sites.

To evaluate the impact of  $\text{TiO}_2$  substrate fracture on conductivity, C-AFM measurements were conducted. Fig. 5c presents the results for the device without  $\text{C}_{60}$  after bending. The dark regions represent non-conductive areas, while the bright regions indicate conductive areas.<sup>50,51</sup> The film without  $\text{C}_{60}$  exhibited an average current level of 2.38 nA. In contrast, when  $\text{C}_{60}$  was incorporated, the film displayed significantly higher conductivity, as shown in Fig. 5d.<sup>52,53</sup> The average current level increased to 6.54 nA. This observation aligns with the previously reported efficiency data for SS-based PSCs, demonstrating a similar trend. These findings indicate that the incorporation of  $\text{C}_{60}$  effectively reduces stress on the  $\text{TiO}_2$  layer during bending, contributing to the maintenance of the device's efficiency under mechanical stress. To further investigate the effects of the  $\text{C}_{60}$  layer on charge extraction and device stability under bending conditions, electrochemical impedance



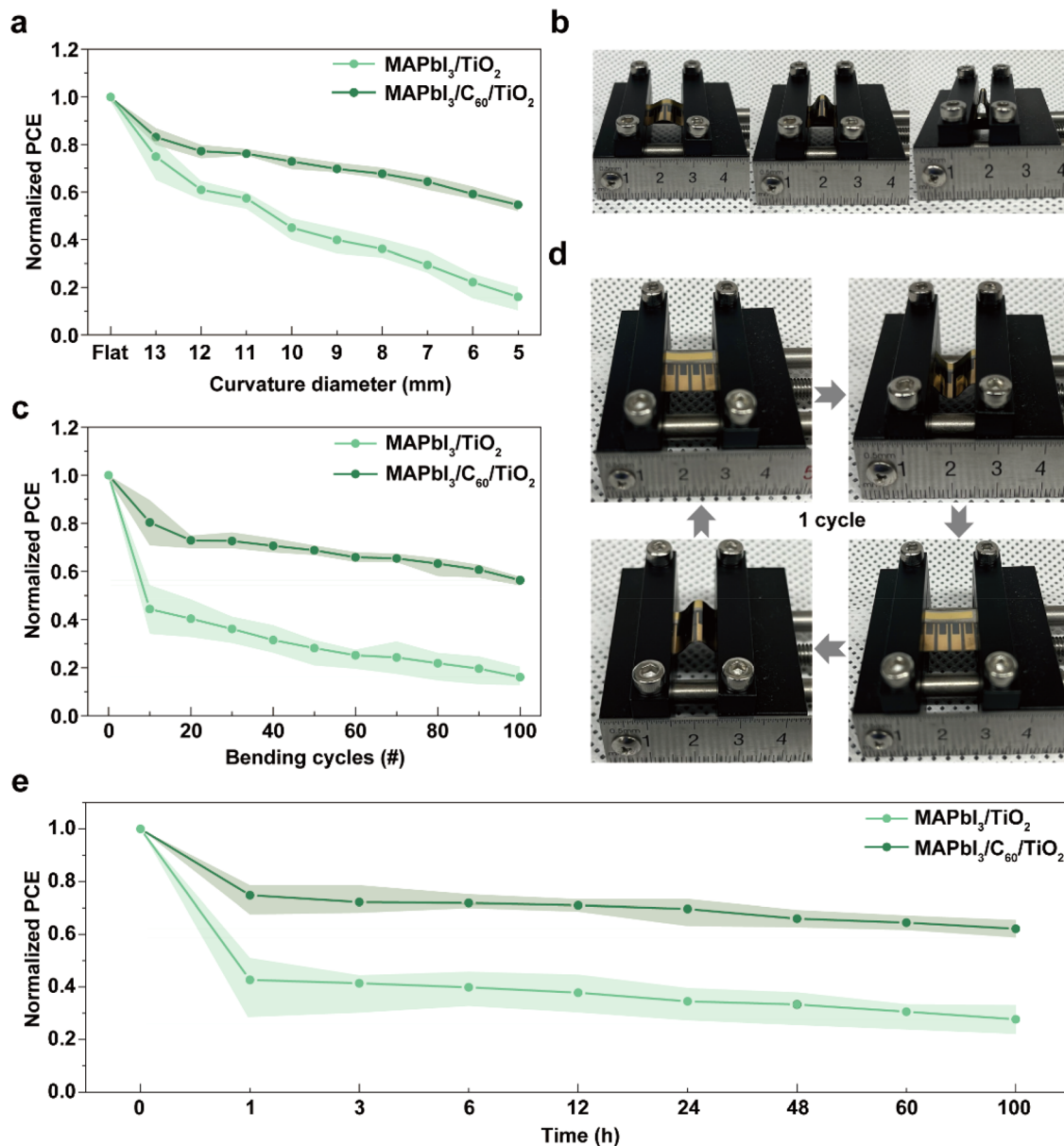


Fig. 6 Stability test of SS-based flexible PSCs after bending: (a) PCE measured after bending the substrate to diameters ranging from flat to 5 mm. (b) Images of devices bent to diameters of 12 mm, 9 mm, and 5 mm. (c) PCE measured over bending cycles ranging from 0 to 100. (d) Images of the devices after 1 bending cycle. (e) PCE measured after bending the substrate within a specified bending time of 0 to 100 h.

spectroscopy (EIS) measurements were performed. The Nyquist plots in Fig. 5e compare the EIS data of devices with and without the C<sub>60</sub> layer before bending. The device with C<sub>60</sub> exhibits a significantly smaller semicircle in the high-frequency region, indicating a reduced charge transfer resistance ( $R_{\text{trans}}$ ). This improvement is attributed to the C<sub>60</sub> layer's ability to enhance charge extraction at the MAPbI<sub>3</sub>/TiO<sub>2</sub> interface by reducing interfacial defects and facilitating efficient electron transport. Furthermore, the semicircle in the low-frequency region, representing recombination resistance ( $R_{\text{rec}}$ ), is notably larger in the device with C<sub>60</sub>. The increased  $R_{\text{rec}}$  demonstrates effective suppression of charge recombination at the interface, contributing to the enhanced performance of the device.<sup>54</sup> Fig. 5f

illustrates the EIS data for devices with and without the C<sub>60</sub> layer after bending. Bending introduces mechanical stress that degrades the TiO<sub>2</sub> layer and increases interfacial defects. For the device without C<sub>60</sub>,  $R_{\text{trans}}$  increases significantly, as evidenced by the enlarged high-frequency semicircle. In contrast, the device with C<sub>60</sub> maintains a relatively smaller  $R_{\text{trans}}$ , emphasizing the protective role of C<sub>60</sub> in preserving charge transport pathways. Additionally, while the low-frequency semicircle ( $R_{\text{rec}}$ ) shrinks for both devices due to increased defect density caused by bending, the reduction in  $R_{\text{rec}}$  is less pronounced in the device with C<sub>60</sub>. This indicates that the C<sub>60</sub> layer mitigates recombination losses even under mechanical stress. These findings confirm that the incorporation of C<sub>60</sub> not only



enhances charge extraction efficiency but also provides improved structural stability to the device under bending conditions. These improvements reflect not only reduced surface stress but also enhanced interfacial integrity and defect tolerance enabled by the  $C_{60}$  layer. By reducing stress concentration factors, facilitating efficient electron transport, and suppressing charge recombination, the  $C_{60}$  layer significantly contributes to the mechanical and operational stability of SS-based PSCs.<sup>54</sup>

To evaluate the morphological and functional stability of  $C_{60}$ -incorporated SS-based PSCs under mechanical deformation, PCE measurements were conducted under various static and dynamic bending conditions. Rather than aiming to extract classical mechanical parameters, this experiment was designed to assess the device performance and interface durability under realistic bending stress. Fig. 6a presents the results of PCE measurements as the bending diameter was adjusted from a flat state to a diameter of 5 mm. The PCE degradation rate was significantly lower in devices with  $C_{60}$  incorporation compared to those without, suggesting enhanced tolerance to bending-induced morphological disruption. Fig. 6b displays images of the devices at bending diameters of 12 mm, 9 mm, and 5 mm, illustrating their structural flexibility under increasing mechanical strain. In the second evaluation, dynamic mechanical stress was applied *via* repeated bending cycles. As shown in Fig. 6c, when the number of bending cycles increased from 0 to 100, devices with  $C_{60}$  incorporation exhibited a markedly lower PCE degradation rate compared to the control. Fig. 6d shows representative images during cyclic deformation. Finally, Fig. 6e illustrates the long-term PCE stability under sustained static bending (10 mm diameter) over 100 hours. Devices with  $C_{60}$  maintained significantly higher PCE values compared to those without  $C_{60}$ , indicating suppressed degradation under prolonged mechanical stress. These results demonstrate that  $C_{60}$  incorporation improves the mechanical reliability of SS-based PSCs not by altering classical stress distributions, but by mitigating localized morphological damage and enhancing interfacial durability under bending.

## Conclusions

This work highlights the dual role of a 20 nm  $C_{60}$  interlayer in SS-based PSCs, demonstrating its contribution to both enhanced mechanical durability and photovoltaic performance under bending stress. The incorporation of  $C_{60}$  shifted the neutral axis closer to the brittle  $TiO_2$  layer and reduced the effective strain and stress by  $\sim 20\%$ , as supported by theoretical and experimental analysis. In addition, the  $C_{60}$  layer reduced  $R_p$ , mitigated the  $K$ , and improved charge extraction efficiency. Importantly,  $C_{60}$  provided structural protection to the electron transport layer while simultaneously enhancing the crystallinity of the active perovskite layer, resulting in greater resilience to mechanical deformation. As a result,  $C_{60}$ -incorporated devices retained 6.2% higher PCE after bending compared to controls. These findings support the use of compliant interfacial layers such as  $C_{60}$  to simultaneously enhance the mechanical

robustness and operational stability of PSCs, which is particularly relevant for emerging applications in BIPV and VIPV.

## Methods

### Materials

SS 304 substrates with a thickness of 0.05T were used. Dimethyl sulfoxide (anhydrous, 99.9%) (DMSO), chlorobenzene (anhydrous, 99.9%), *N,N*-dimethylformamide (anhydrous, 99.8%) (DMF), acetonitrile (anhydrous, 99.8%), fullerene- $C_{60}$ , lead(II) iodide ( $PbI_2$ ), diethyl ether, 4-*tert*-butylpyridine (96%), and lithium bis(trifluoromethanesulfonyl)imide (Li-TFSI) were purchased from Sigma-Aldrich. Methylammonium iodide (MAI) was procured from dyesol, and 2,2',7,7'-tetrakis [*N,N*-di(4-methoxyphenyl)amino]-9,9'-spirobifluorene (spiro-OMeTAD) was obtained from Lumtec.

### Fabrication of perovskite solar cell

The SS substrates were sequentially cleaned by sonication in acetone, ethanol, and isopropanol for 15 minutes each. Subsequently, the substrates were treated with ultraviolet (UV)-ozone for 30 minutes. To serve as a diffusion barrier, a 1  $\mu m$  layer of  $SiO_2$  was deposited onto the SS substrates *via* plasma-enhanced chemical vapor deposition (PECVD). The  $TiO_2$  layer, with a target thickness of 50 nm, was fabricated through RF magnetron sputtering at a chamber pressure below  $7 \times 10^{-7}$  mTorr.  $C_{60}$  layers were deposited by thermal evaporation at varying thicknesses of 5, 10, 20, and 30 nm. A 1 M perovskite precursor solution was prepared by dissolving stoichiometric amounts of  $PbI_2$  and MAI in a 1 : 1 (v/v) mixture of DMSO and  $\gamma$ -butyrolactone (GBL). The solution was stirred at 70 °C for 2 hours and filtered using a 0.2  $\mu m$  PTFE syringe filter. Subsequently, the solution was deposited onto the substrate using a two-step spin-coating process: 1000 rpm for 10 seconds, followed by 5000 rpm for 60 seconds. During the second step, 1000  $\mu L$  of chlorobenzene was dropped onto the center of the perovskite film as an antisolvent to facilitate the crystallization of perovskite grains. The substrate was annealed at 100 °C for 1 hour to complete the crystallization of the perovskite layer. For the hole transport layer (HTL), spiro-OMeTAD powder was dissolved in a solution containing 28.8  $\mu L$  of 4-*tert*-butylpyridine, 520 mg of Li-TFSI in 1 mL of acetonitrile, and 1 mL of chlorobenzene. The prepared solution was applied onto the substrate and spin-coated to form a thin layer. A 10 nm thick  $MoO_x$  buffer layer was then thermally evaporated, followed by the deposition of a 160 nm thick ITO transparent electrode using RF magnetron sputtering. Finally, a 100 nm thick Au electrode was deposited through thermal evaporation.

### Materials characterization

Scanning electron microscopy (SEM) was performed using a Quanta 250 FEG microscope (FEI). X-ray diffraction (XRD) patterns were obtained using an X-ray diffractometer (Rigaku) with Cu-K $\alpha$  radiation ( $\lambda = 1.54$  Å). X-ray photoelectron spectroscopy (XPS) measurements were conducted with a Thermo Scientific K-Alpha system equipped with a monochromated Al





K $\alpha$  X-ray source. Photoluminescence (PL) spectra were measured on a JASCO FP-8500 spectrofluorometer. Lifetime measurements were carried out using a 470 nm picosecond laser (PicoQuant, Germany) as the excitation source. Atomic force microscopy measurements were performed using a Dimension 3 Edge AFM system (Bruker). Conductive atomic force microscopy (C-AFM) was employed to measure conductivity using the Dimension Edge C-AFM system.

### Device characterization

A class AAA solar simulator was used to measure the  $J$ - $V$  characteristics of the devices at a scanning rate of  $0.05 \text{ V s}^{-1}$ , using a Keithley 2400 instrument. The AM 1.5G (1 sun,  $100 \text{ mW cm}^{-2}$ ) solar power was calibrated using a silicon reference solar cell. All  $J$ - $V$  measurements were performed with a  $0.075 \text{ cm}^2$  mask, and the scan voltage setting time was 200 ms. The incident photon-to-current conversion efficiency (IPCE) was measured using equipment from HS Technology Inc. Electrochemical impedance spectroscopy measurements were conducted under simulated AM 1.5G illumination at an intensity of  $1 \text{ mA cm}^{-2}$  using an electrochemical measurement system (InViumStat.XR, InVium Technologies). EIS measurements were performed over a frequency range of 1 Hz to 1 MHz.

### Data availability

The data supporting this article have been included as part of the ESI.†

### Author contributions

H.-S. Lee and D. H. Kim supervised the overall project. H. J. Lee and K. Kim were responsible for developing concrete strategies, data curation, formal analysis, investigation, and writing the original draft and editing. S. Lee and D. Pyun performed data curation and formal analysis. J.-S. Hwang, J. Nam, S. Cho, and S.-H. Jeong performed formal analysis. D. Kim and Y. Kang performed project administration. All authors have read and approved the manuscript.

### Conflicts of interest

There are no conflicts to declare.

### Acknowledgements

This work was supported by the Korea Institute of Energy Technology Evaluation and Planning (KETEP) grant funded by the Korea government(MOTIE) (RS-2024-00451343). This work was supported by Basic Science Research Program (Priority Research Institute) through the NRF of Korea funded by the Ministry of Education (2021R1A6A1A10039823).

### References

- W. Yue, H. Yang, H. Cai, Y. Xiong, T. Zhou, Y. Liu, J. Zhao, F. Huang, Y.-B. Cheng and J. Zhong, *Adv. Mater.*, 2023, **35**, 2301548.
- A. Chatzipanagi, G. Kakoulaki, S. Szabó and A. Jäger-Waldau, *Appl. Sci.*, 2024, **14**, 10628.
- T. E. Kuhn, C. Erban, M. Heinrich, J. Eisenlohr, F. Ensslen and D. H. Neuhaus, *Energy Build.*, 2021, **231**, 110381.
- B. Commault, T. Duigou, V. Maneval, J. Gaume, F. Chabuel and E. Voroshazi, *Appl. Sci.*, 2021, **11**, 11598.
- B. T. Feleki, R. K. M. Bouwer, V. Zardetto, M. M. Wienk and R. A. J. Janssen, *ACS Appl. Energy Mater.*, 2022, **5**, 6709.
- S. Lee, S.-W. Lee, S. Bae, J.-K. Hwang, W. Lee, D. Pyun, S.-H. Jeong, K. Kim, J.-S. Hwang, S. Cho, D. Kim, Y. Kang and H.-S. Lee, *Energies*, 2023, **16**, 8061.
- J. Zheng, F.-J. Ma, C. Liao, J. Bing, S. Tang, A. M. Soufiani, R. L. Chin, C. Xue, J. Qu, L. Yang, M. A. Mahmud, Z. Sun, T. L. Leung, G. Wang, J. M. Cairney, S. Bremner, D. R. McKenzie, S. Huang and A. W. Y. Ho-Baillie, *Cell Rep. Phys. Sci.*, 2023, **4**, 101543.
- C. Zhou, Y. Xu, Y. Li, K. Du, X. Li, X. Dong, L. Li, N. Yuan and J. Ding, *Sol. RRL*, 2024, **8**, 2300901.
- K. Ahn, S.-Y. Kim, S. Kim, D.-H. Son, S.-H. Kim, S. Y. Kim, J. H. Kim, S.-J. Sung, D.-H. Kim and J.-K. Kang, *J. Mater. Chem. A*, 2019, **7**, 24891.
- K. H. Jung, S. J. Yun, S. H. Lee, Y. J. Lee, K.-S. Lee, J. W. Lim, K.-B. Kim, M. Kim and R. E. I. Schropp, *Sol. Energy Mater. Sol. Cells*, 2016, **145**, 368.
- L. Kranz, C. Gretener, J. Perrenoud, R. Schmitt, F. Pianezzi, F. L. La Mattina, P. Blösch, E. Cheah, A. Chirilă, C. M. Fella, H. Hagedorfer, T. Jäger, S. Nishiwaki, A. R. Uhl, S. Buecheler and A. N. Tiwari, *Nat. Commun.*, 2013, **4**, 2306.
- K. Miettinen, J. Halme, M. Toivola and P. Lund, *J. Phys. Chem. C*, 2008, **112**, 4011.
- J. Liu, Z. Zhao, J. Qian, Z. Liang, C. Wu, K. Wang, S. Liu and D. Yang, *Adv. Mater.*, 2024, **36**, 2401236.
- J. Liu, T. Ye, D. Yu, S. Liu and D. Yang, *Angew. Chem., Int. Ed.*, 2023, **62**, e202307225.
- Y. Ma, Z. Lu, X. Su, G. Zou and Q. Zhao, *Adv. Energy Syst. Res.*, 2023, **4**, 2200133.
- J. Zhang, W. Zhang, H.-M. Cheng and S. R. P. Silva, *Mater. Today*, 2020, **39**, 66.
- Z. Li, C. Jia, J. Cao, J. Shi, J. Xue, X. Liu, H. Wu, C. Xiao, C. Li, M. Li, C. Zhang and Z. Li, *Nat. Commun.*, 2025, **16**, 1771.
- D. A. Chalkias, A. Nikolakopoulou, L. C. Kontaxis, A. N. Kalarakis and E. Stathatos, *Adv. Funct. Mater.*, 2024, **34**, 2406354.
- L. Dong, S. Qiu, J. G. Cerrillo, M. Wagner, O. Kasian, S. Feroze, D. Jang, C. Li, V. M. L. Corre, K. Zhang, H. Peisert, F. U. Kosasih, C. Ducati, C. Arrive, T. Du, F. Yang, C. J. Brabecm and H.-J. Egelhaaf, *Energy Environ. Sci.*, 2024, **17**, 7091–7106.



- 20 W. Xu, B. Chen, Z. Zhang, Y. Liu, Y. Xian, X. Wang, Z. Shi, H. Gu, C. Fei, N. Li, M. A. Uddin, H. Zhang, L. Dou, Y. Yan and J. Huang, *Nat. Protoc.*, 2024, **18**, 379.
- 21 H. Liang, W. Yang, J. Xia, H. Gu, X. Meng, G. Yang, Y. Fu, B. Wang, H. Cai, Y. Chen, S. Yang and C. Liang, *Adv. Sci.*, 2023, **10**, 2304733.
- 22 X. Hu, Z. Huang, X. Zhou, P. Li, Y. Wang, Z. Huang, M. Su, W. Ren, F. Li, M. Li, Y. Chen and Y. Song, *Adv. Mater.*, 2017, **29**, 1703236.
- 23 G. Lee, M.-C. Kim, Y. W. Choi, N. Ahn, J. Jang, J. Yoon, S. M. Kim, J.-G. Lee, D. Kang, H. S. Jung and M. Choi, *Energy Environ. Sci.*, 2019, **12**, 3182.
- 24 H. P. Parkhomenko, Y. Yerlanuly, V. V. Brus and A. N. Jumabekov, *Org. Electron.*, 2024, **129**, 107049.
- 25 N. Rolston, K. A. Bush, A. D. Printz, A. Gold-Parker, Y. Ding, M. F. Toney, M. D. McGehee and R. H. Dauskardt, *Adv. Energy Mater.*, 2018, **8**, 1802139.
- 26 Q. Dong, M. Chen, Y. Liu, F. T. Eickemeyer, W. Zhao, Z. Dai, Y. Yin, C. Jiang, J. Feng, S. Jin, S. Liu, S. M. Zakeeruddin, M. Grätzel, N. P. Padture and Y. Shi, *Joule*, 2021, **5**, 1587.
- 27 Y. Guo, J. Cheng, L. Liu and Z. Tan, *Mater. Lett.*, 2021, **292**, 129559.
- 28 A. A. Alsayed, *J. Appl. Math. Phys.*, 2021, **9**, 176.
- 29 C. Wang, L. Ma, D. Guo, X. Zhao, Z. Zhou, D. Lin, F. Zhang, W. Zhao, J. Zhang and Z. Nie, *J. Mater. Chem. C*, 2020, **8**, 3374.
- 30 S. F. Wen, W. Z. Yan, J. X. Kang, J. Liu and Z. F. Yue, *Appl. Surf. Sci.*, 2010, **257**, 1289.
- 31 R. Saleh, M. Barth, W. Eberhardt and A. Zimmermann, *Micromachines*, 2021, **12**, 78.
- 32 B. Li, X. Wu, H. Zhang, S. Zhang, Z. Li, D. Gao, C. Zhang, M. Chen, S. Xiao, A. K.-Y. Jen, S. Yang and Z. Zhu, *Adv. Funct. Mater.*, 2022, **32**, 2205870.
- 33 X. Yu, W. Ge, L. Fan, B. Fan, R. Peng and B. Jin, *J. Colloid Interface Sci.*, 2023, **650**, 553.
- 34 K.-W. Tsai, C.-C. Chueh, S. T. Williams, T.-C. Wen and A. K. Y. Jen, *J. Mater. Chem. A*, 2015, **3**, 9128.
- 35 L.-C. Chen, Y.-S. Lin, Z.-L. Tseng, C. Wu, F.-S. Kao and S.-H. Chen, *Nanomaterials*, 2017, **7**, 166.
- 36 N. Klipfel, A. O. Alvarez, H. Kanda, A. A. Sutanto, C. Igci, C. Roldán-Carmona, C. Momblona, F. Fabregat-Santiago and M. K. Nazeeruddin, *ACS Appl. Energy Mater.*, 2022, **5**, 1646.
- 37 H.-S. Lin, I. Jeon, R. Xiang, S. Seo, J.-W. Lee, C. Li, A. Pal, S. Manzhos, M. S. Goorsky, Y. Yang, S. Maruyama and Y. Matsuo, *ACS Appl. Mater. Interfaces*, 2018, **10**, 39590.
- 38 Y.-Q. Zhou, B.-S. Wu, G.-H. Lin, Z. Xing, S.-H. Li, L.-L. Deng, D.-C. Chen, D.-Q. Yun and S.-Y. Xie, *Adv. Energy Mater.*, 2018, **8**, 1800399.
- 39 F. Ye, S. Zhang, J. Warby, J. Wu, E. Gutierrez-Partida, F. Lang, S. Shah, E. Saglamkaya, B. Sun, F. Zu, S. Shoaee, H. Wang, B. Stiller, D. Neher, W.-H. Zhu, M. Stollerfoht and Y. Wu, *Nat. Commun.*, 2022, **13**, 7454.
- 40 V. Arivazhagan, J. Xie, P. Hang, M. M. Manonmani Parvathi, A. Khan, C. Cui, D. Yang and X. Yu, *J. Phys. D*, 2019, **52**, 225104.
- 41 J. Y. Kim, J.-W. Lee, H. S. Jung, H. Shin and N.-G. Park, *Chem. Rev.*, 2020, **120**, 7867.
- 42 D. Liu, Q. Wang, C. J. Traverse, C. Yang, M. Young, P. S. Kuttipillai, S. Y. Lunt, T. W. Hamann and R. R. Lunt, *ACS Nano*, 2018, **12**, 876.
- 43 P.-W. Liang, C.-C. Chueh, S. T. Williams and A. K.-Y. Jen, *Adv. Energy Mater.*, 2015, **5**, 1402321.
- 44 K. Wojciechowski, S. D. Stranks, A. Abate, G. Sadoughi, A. Sadhanala, N. Kopidakis, G. Rumbles, C.-Z. Li, R. H. Friend, A. K.-Y. Jen and H. J. Snaith, *ACS Nano*, 2014, **8**, 12701.
- 45 S. Moore, R. Burrows, D. Kumar, M. B. Kloucek, A. D. Warren, P. E. J. Flewitt, L. Picco, O. D. Payton and T. L. Martin, *npj Mater. Degrad.*, 2021, **5**, 3.
- 46 Y. Zhao, W. Zhou, W. Ma, S. Meng, H. Li, J. Wei, R. Fu, K. Liu, D. Yu and Q. Zhao, *ACS Energy Lett.*, 2016, **1**, 266.
- 47 Y. Li, Y. Zhao, Q. Chen, Y. M. Yang, Y. Liu, Z. Hong, Z. Liu, Y.-T. Hsieh, L. Meng, Y. Li and Y. Yang, *J. Am. Chem. Soc.*, 2015, **137**, 15540.
- 48 D. Arola and C. L. Williams, *Int. J. Fatig.*, 2002, **24**, 923.
- 49 W. D. Pilkey, D. F. Pilkey and Z. Bi, *Peterson's Stress Concentration Factors*, Wiley, Hoboken, NJ, 4th edn, 2020.
- 50 H. Si, S. Zhang, S. Ma, Z. Xiong, A. Kausar, Q. Liao, Z. Zhang, A. Sattar, Z. Kang and Y. Zhang, *Adv. Energy Mater.*, 2020, **10**, 1903922.
- 51 M. Kim, J. Kwon, H. J. Lee, K. S. Park, J. Kim, J. Kim, K. Baek, H. Yuan, J. K. Hyun, Y. S. Cho, J. Yeom and D. H. Kim, *Nano Energy*, 2023, **114**, 108680.
- 52 C. Guo, J. Chen, G. Li, X. Liang, W. Lai, L. Yang, Y. Mai and Z. Li, *Glob. Chall.*, 2019, **3**, 1800108.
- 53 A. A. Said, E. Aydin, E. Ugur, Z. Xu, C. Deger, B. Vishal, A. Vlk, P. Dally, B. K. Yildirim, R. Azmi, J. Liu, E. A. Jackson, H. M. Johnson, M. Gui, H. Richter, A. R. Pininti, H. Bristow, M. Babics, A. Razzaq, S. Mandal, T. G. Allen, T. D. Anthopoulos, M. Ledinský, I. Yavuz, B. P. Rand and S. De Wolf, *Nat. Commun.*, 2024, **15**, 708.
- 54 L. Chen, C. Xu, Y. Qin, X. He, H. Bian, G. Xu, L. Niu and Q. Song, *Nanomaterials*, 2022, **12**, 1736.

